MEASUREMENT AND CALCULATION OF THE RAMAN OPTICAL ACTIVITY OF α-PINENE AND *trans*-PINANE

Petr BOUR[a], Vladimir BAUMRUK[b1] and Jana HANZLIKOVA[b2]

[a] *Institute of Organic Chemistry and Biochemistry, Academy of Sciences of the Czech Republic, 166 10 Prague 6, Czech Republic; e-mail: bour@uochb.cas.cz*

[b] *Institute of Physics, Charles University, 121 16 Prague 2, Czech Republic; e-mail: [1] baumruk@karlov.mff.cuni.cz, [2] hanzliko@karlov.mff.cuni.cz*

Received January 13, 1997
Accepted April 1, 1997

Raman scattering and Raman optical activity (ROA) spectra of α-pinene and *trans*-pinane were measured for both enantiomers. The experiment was performed on a newly built, fully computer-controlled backscattering incident circular polarization ROA instrument. High-quality spectra were obtained and interpreted on the basis of *ab initio* quantum chemical calculations. Excellent agreement between the calculated and observed spectra was observed in the mid IR region. An approximate distributed origin gauge model for calculation of the polarization tensors was proposed. The shapes of ROA spectra calculated with this model are similar to those obtained with conventional, computationally more demanding ROA computations.

Key words: Raman optical activity; *Ab initio* calculations.

Raman optical activity is the differential response of a chiral molecule to right- and left-circularly polarized light (CPL)

$$\Delta I = I_R - I_L \,, \qquad (1)$$

where I_R and I_L are scattered intensities with respect to right- and left-CPL, respectively. Although ROA represents a relatively new area of spectroscopy, many experimental techniques have been developed and the method has been applied on a wide range of molecules, including biologically important molecules such as proteins and nucleic acids[1]. The relation of ROA spectra to molecular structure is well documented both experimentally and in theoretical studies. Nevertheless, many problems have to be solved before the method can be used as NMR or X-ray spectroscopies for structural analysis. Calculations of ROA are extremely demanding with respect to computer time and memory. For biopolymers, the experimental signal is often weak or not resolved. However, for the medium-sized molecules presented here the spectrum–structure relationship is well established.

The availability and strong VCD and ROA signals of terpenes permits their use as standard "calibration" compounds for vibrational circular dichroism (VCD) and ROA spectrometers[2]. The aim of this study is to compare performance of our newly-built ROA spectrometer with ROA instruments reported previously. Moreover, new *ab initio* methods were implemented for the interpretation of Raman and ROA spectra, including the use of density functional theory (DFT) and Cartesian tensor transfer[3]. According to our knowledge similar *ab initio* calculations of ROA spectra for the two molecules have not been yet reported.

Detailed theory of Raman optical activity can be found elsewhere[4]. The main obstacle in *ab initio* simulations of ROA spectra is the numerical calculation of the derivatives of the optical activity tensor[1,5], which requires solving the Hartree–Fock equations coupled with an external magnetic field $3N$ times, where N is the number of atoms. An analytical method, based on second derivatives of the electronic wave function according to external magnetic field and nuclear motion, is not currently available. Thus the calculation of ROA intensities is very demanding with respect to the computer time. On the contrary, *ab initio* calculations of sole Raman intensities (*i.e.* electric polarizability derivatives) have been implemented analytically on the basis of coupled HF equations[6], and the computer cost is comparable with the calculations of molecular harmonic force fields.

Another complications that arise during ROA intensity calculations originate in the nature of magnetic properties, and can be encountered in simulations of vibrational circular dichroism (VCD) or NMR shieldings. Magnetically-perturbed Fock matrices lead to complex wave functions and the results are generally dependent on the choice of the origin of the coordinates. To avoid these problems, many simplifying models for ROA have been proposed previously[7]. The two-group and the bond polarizability models completely eliminate the magnetic dipole operator $\vec{m}$ from the resultant equations, using its dependence on the shift of the coordinate system:

$$\vec{m}(0) = -(1/2)\vec{a} \times (\partial \vec{\mu} / \partial t) \,. \qquad (2)$$

Thus a magnetic moment at the origin, $\vec{m}(0)$, can be formally replaced by the time derivative of the electric dipole moment, $\vec{\mu}$, shifted by $\vec{a}$ from the origin. In our model we take advantage of the Eq. (*2*), but the magnetic part does not vanish completely. A distributed origin gauge is used to construct the part of the optical activity tensor from the electric polarizability[3]. This procedure substantially reduces computational time, since the electric derivatives can be calculated at a higher level of approximation than the magnetic derivatives and are origin-independent.

EXPERIMENTAL

The fully computer-controlled backscattering incident circular polarization[4] (ICP) ROA spectrometer built in our laboratory follows the design of the instrument constructed by Barron's group in Glasgow[8]. The optical layout of the spectrometer is depicted schematically in Fig. 1.

As an excitation source, a single-line operated continuous-wave Argon ion laser (Coherent, Innova 305) is employed. To suppress plasma radiation an interference 514.5 nm filter is placed in front of the laser head. An air-spaced calcite Glan–Taylor prism polarizer (GT 10, Leysop) with a single-layer antireflection coatings on both faces, follows the interference filter to improve the polarization of the laser beam.

An improved linearly polarized radiation emerging from the prism polarizer passes through a Leysop EM 565 electro-optic modulator (EOM), a longitudinal Pockels cell based on a potassium dideuteriumphosphate (KD*P) crystal. The crystal is encapsulated in an oven to eliminate birefringence drifts caused by external temperature changes. The oven temperature (set typically to 30 °C) is stabilized (±0.1 °C) using a temperature controller modulator (CAL 3200). The EOM is mounted on micrometer-driven translation, rotation (Newport URM80A) and inclination (Newport TGN80) stages that permit alignment of the central axis of the EOM crystal exactly along the laser beam and to orient the fast axis precisely at 45° with respect to the plane of the polarization of the incident radiation. The EOM is driven by a high-voltage linear differential amplifier (Leysop model 5000). Right and left circular polarization states are generated by applying the appropriate quarter-wave voltages across the EOM electrodes. Positive and negative input potential (in the range of 0–2.5 V with 2.5 mV resolution) is provided by a custom-built low voltage power supply which is controlled from a personal computer by means of two TTL signals (the first one for the positive and the second one for the negative input voltage).

The circularly polarized beam is focused by a plan-convex synthetic fused-silica lens (150 mm focal length, 25 mm diameter, Melles–Griot 01LQP013) into a standard glass cell containing approximately 300 μl of the sample. The sample cell is mounted on a precision XYZ translation stage. Before the sample is reached, the focused laser beam passes through holes (2 mm diameter) drilled in a plane elliptical mirror, a collimating lens and a Lyot depolarizer.

The backscattered Raman radiation emerging from the sample penetrates the Lyot depolarizer (Leysop) that consists of 3.5 and 7 mm thick calcite plates, held together by optical cement, with optical axes oriented at 45 ± 0.2° with respect to each other. Both the entrance and exit faces of the depolarizer are coated by a single antireflection layer. The depolarized scattered light is collimated

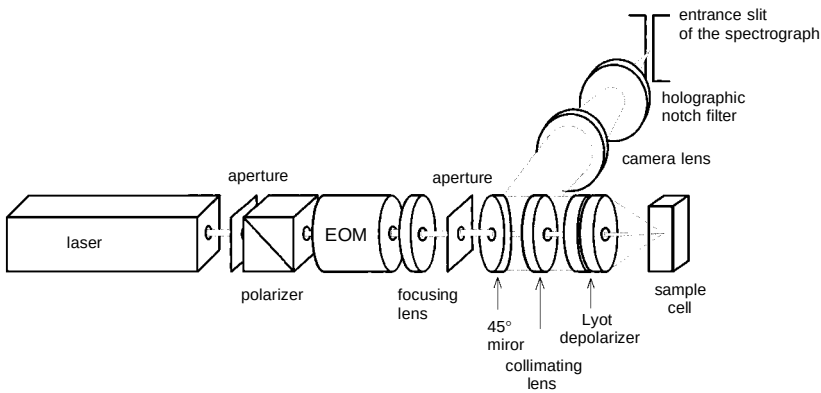

FIG. 1
Optical layout of the ROA spectrometer

by a f/1.0 25 mm symmetric convex fused-silica lens. Both the depolarizer and the collimating lens are mounted in a precision polarizer holder (Melles–Griot 07-HPT-001) with the reading angle accuracy of five minutes. The collimated scattered radiation is deflected by 90° with a plane elliptical mirror (35.4 × 25.0 mm).

After the collimation and deflection, the scattered light is focused by a 1.8/80 camera lens (Pancolar, Zeiss Jena) onto an entrance slit of a spectrograph (Monospek 600, Hilger&Watts) equipped with a plane holographic reflection grating (Milton Roy) having 1 200 grooves/mm. A tilted holographic notch filter (Kaiser Optical Systems) is placed in front of the entrance slit to effectively block the Rayleigh scattering (optical density >6.0 at 514.5 nm). The spectrograph disperses the light along the longer axis of a liquid nitrogen cooled CCD detector (Princeton Instruments, EEV chip having 1 024 × 256 pixels). The spectrograph provides a reciprocal linear dispersion of 1.2 nm/mm at 500 nm and a resolution of about 5 cm^{-1} for a slit 100 μm wide. With a 514.5 nm excitation one can measure Raman spectra over a spectral interval wide of about 1 250 cm^{-1}.

The ROA acquisition mode is based on a Spectrum Basic program running under a standard CSMA software package (Princeton Instruments). The program allows both Raman ($I_R + I_L$) and ROA ($I_R - I_L$) spectra to be displayed after each measurement cycle[9].

Samples of both enantiomeric forms of *trans*-pinane and α-pinene were purchased from Fluka and Aldrich, respectively, and studied as neat liquids.

THEORETICAL

The structure and (arbitrary) atom numbering for (1*S*)-(–)-α-pinene and (–)-*trans*-pinane can be seen in Figs 2a and 2b. The geometries were optimized and second energy derivatives were calculated using the Gaussian 94 set of programs[10]. The calculations were performed at the Becke3LYP level[11,12] with the 6-31G** basis set. The combination of this DFT functional with the 6-31G** basis set has been tested on a wide range

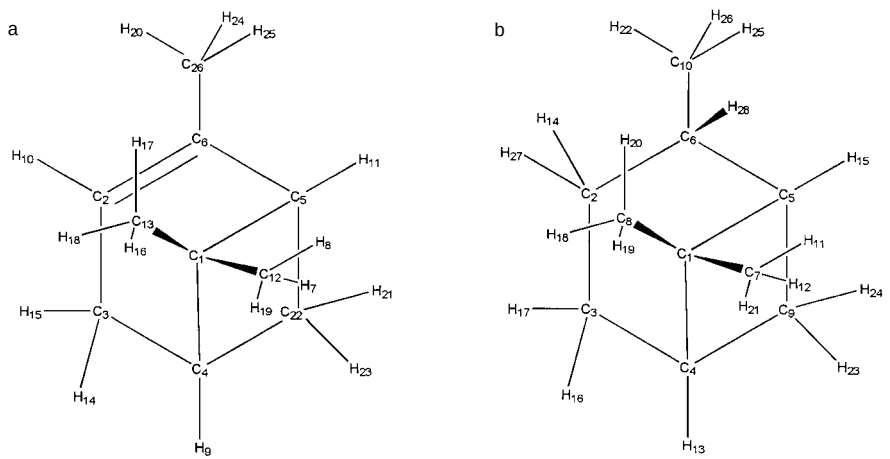

FIG. 2
Structures and atom numbering of (1*S*)-(–)-α-pinene (a) and (–)-*trans*-pinane (b) with the atomic numberings used for the calculations

of organic molecules, and calculated vibrational frequencies usually agree within an error of few percent with experiment[13,14].

Calculation of the polarizability derivatives is not implemented at the Becke3LYP level in Gaussian 94, thus the derivatives had to be calculated at the lower HF/6-31G** level.

For calculation of the derivatives of the electric dipole–electric quadrupole polarizability, $\boldsymbol{A}$, and the electric dipole–magnetic dipole polarizability ("optical activity tensor"), $\boldsymbol{G'}$, the origin dependence (*2*) was used, allowing to express the tensors as[3,7]

$$(\partial/\partial x_\varepsilon^\lambda)G'_{\alpha\beta}(0) = (\partial/\partial x_\varepsilon^\lambda)G'_{\alpha\beta}(\lambda) - (\omega/2)\varepsilon_{\beta\gamma\delta}R_\gamma^\lambda(\partial/\partial x_\varepsilon^\lambda)\alpha_{\alpha\delta}(0) \qquad (3)$$

$$(\partial/\partial x_\varepsilon^\lambda)A_{\alpha,\beta\gamma}(0) = (\partial/\partial x_\varepsilon^\lambda)A_{\alpha,\beta\gamma}(\lambda) + 3/2[R_\beta^\lambda(\partial/\partial x_\varepsilon^\lambda)\alpha_{\alpha\gamma}(0) + R_\gamma^\lambda(\partial/\partial x_\varepsilon^\lambda)\alpha_{\alpha\beta}(0)] -$$
$$- R_\delta^\lambda(\partial/\partial x_\varepsilon^\lambda)\alpha_{\alpha\delta}(0)\delta_{\beta\gamma}\,, \qquad (4)$$

where $\partial/\partial x_\varepsilon^\lambda$ denotes the derivative according to the ε-coordinate of the atom λ. The Einstein summation convention is used here (an index occurring twice in a product is summed over). $\boldsymbol{R}^\lambda$ is the equilibrium position of the atom λ and tensor α(0) is the electric dipole–electric dipole polarizability. The zero and λ in the parentheses indicates that the tensor is expressed in the common origin and the origin on atom λ, respectively. Note, that while $\alpha(0) = \alpha(\lambda)$, $\boldsymbol{G'}(0) \neq \boldsymbol{G'}(\lambda)$ and $\boldsymbol{A}(0) \neq \boldsymbol{A}(\lambda)$. For definition of tensors see refs[2,7].

Since the calculation of the magnetic properties is the most difficult part, the local contributions $(\partial/\partial x_\varepsilon^\lambda)G'_{\alpha\beta}(\lambda)$ and $(\partial/\partial x_\varepsilon^\lambda)A_{\alpha,\beta\gamma}(\lambda)$ were set to zero as a first approximation. We will refer to this approach as the polarization model (Calculation II later in the Fig. 3).

Spectral intensities were calculated for each normal mode *I* for

Raman

$$I_R + I_L = K(7\alpha_{\alpha\beta}^{(I)}\alpha_{\alpha\beta}^{(I)} + \alpha_{\alpha\alpha}^{(I)}\alpha_{\beta\beta}^{(I)}) \qquad (5)$$

ROA_{180}

$$I_R - I_L = K(8\omega/c)\,[\omega^{-1}(3\alpha_{\alpha\beta}^{(I)}G'^{(I)}_{\alpha\beta} - \alpha_{\alpha\alpha}^{(I)}G'^{(I)}_{\beta\beta}) + 1/3\varepsilon_{\alpha\beta\gamma}\alpha_{\alpha\delta}^{(I)}A_{\beta,\gamma\delta}^{(I)}]\,, \qquad (6)$$

where ω is the frequency of the incident radiation, *c* is the velocity of the light and the upper index (*I*) denotes the derivative according to the normal mode *I*. The normal mode derivatives are related to the Cartesian derivatives *via* the normal mode displacement matrix, $\boldsymbol{S}$, as $\alpha_{\alpha\beta}^{(I)} = S_{\varepsilon,I}^\lambda(\partial/\partial x_\varepsilon^\lambda)\alpha_{\alpha\beta}^\lambda$, *etc*. A set of programs was used for the transformations (*3*)–(*4*) as well as for the calculation of spectral intensities[3].

To improve the overall profile, the absolute differential Raman scattering cross section[15] was calculated as

$$\partial\sigma_I/\partial\Omega = k(\omega - \omega_I)^4 \left\{\omega_I \left[1 - \exp\left(-\hbar\omega_I/(k_B T)\right)\right]\right\}^{-1} I_I \ , \qquad (7)$$

where ω_I is the excitation frequency, $\hbar$ is Planck constant, k_B the Boltzmann constant, T the temperature, k a constant independent of frequency and I_I the intensity calculated according to Eqs (*5*) and (*6*).

To obtain the local magnetic and electric quadrupole contributions (see Eqs (*3*) and (*4*)) to the spectrum, Cartesian derivatives of $\boldsymbol{G'}$ and $\boldsymbol{A}$ were calculated by the finite difference method at a lower level of approximation, HF/4-31G. The geometry was consistent (Becke3LYP/6-31G** optimized) throughout the calculation. The local parts of the tensors were combined with the HF/6-31G** derivatives and the Becke3LYP/6-31G** force field, and the spectral intensities were calculated. The tensors were transferred in Cartesian coordinates using software described recently[3]. This is referred to as Calculation I in Fig. 3.

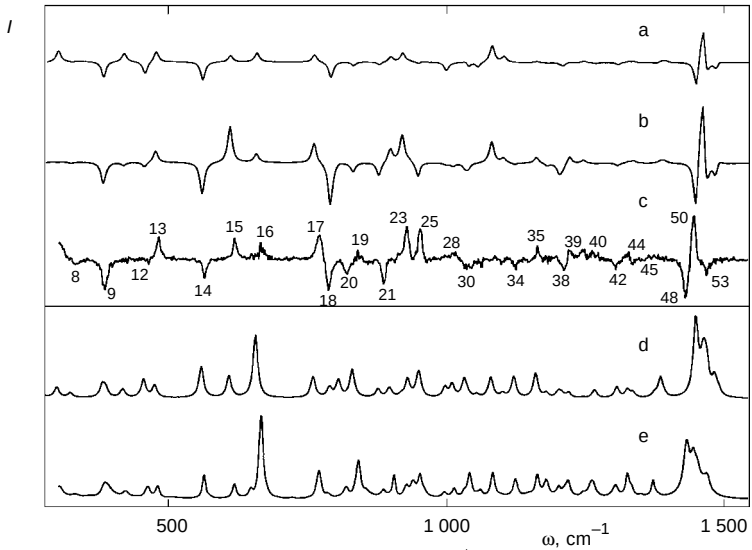

FIG. 3

Raman optical activity and Raman intensity spectra of (1*S*)-(–)-α-pinene. a ROA spectra calculated using the electric polarizability derivatives only (Calculation II); b with the local magnetic and electric quadrupole contributions included (Calculation I); c experimental ROA spectrum; d simulated and e experimental Raman spectra. The most intense peaks are numbered in experimental ROA spectra for easier orientation, see Tables I and II

TABLE I
Calculated and experimental vibrational frequencies of α-pinene (C–H stretching modes excluded)

Mode	ω_{CAL}[a], cm^{-1}	ω_{EXP}, cm^{-1}	Mode description[b]
56	1 687.00		C=C stretch; C6(100), C26(84)
55	1 492.69		CH3 bend; H18(100), H17(71)
54	1 485.51	1 470.00	CH3 bend; H23(100), H19(91), H21(90), H7(60)
53	1 471.73	1 458.00	CH3 bend; H17(100), H16(87), H23(83), H21(78)
52	1 466.71	1 454.00	CH3 bend; H7(100), H8(85)
51	1 463.32	1 447.00	CH3 bend; H25(100), H20(95)
50	1 456.68	1 442.00	CH3 bend; H16(100), H19(73), H17(56)
49	1 452.23	1 434.00	CH3 bend; H24(100), H20(48)
48	1 451.00	1 432.00	CH2 bend; H15(100), H4(98)
47	1 395.32	1 382.50	CH3 bend; H8(100), H19(99), H16(98), H7(84)
46	1 388.62	1 376.00	CH3 bend; H20(100), H25(99), C26(82)
45	1 377.82	1 364.50	CH3 bend; H16(100), H8(83), H17(83), H19(83)
44	1 338.80	1 331.50	CH bend; H9(100), C3(94)
43	1 329.06	1 328.00	CH bend; C6(100), C5(89), H11(86)
42	1 309.82	1 307.00	CH bend; H10(100), C3(82)
41	1 270.01	1 265.00	CH bend; C4(100), H9(99), C1(98)
40	1 248.66	1 249.50	CH bend; H11(100), H23(99), H10(81)
39	1 222.98	1 222.00	CH2 wagging; H21(100), C22(53)
38	1 210.46	1 212.00	CH bend; C1(100), H9(18)
37	1 204.27	1 205.00	CH bend + ring def.; C1(100), H14(72)
36	1 182.32	1 185.00	CH bend + ring def.; C1(100), H11(50)
35	1 163.06	1 166.00	C–CH_3 stretch; C6(100), H11(67)
34	1 123.21	1 132.00	CH bend; H11(100), C6(55)
33	1 103.14	1 126.00	CH bend; H9(100), H11(79)
32	1 081.88	1 085.00	CH bend + ring def.; H23(100), H21(68)
31	1 056.79	1 064.00	CH bend; H15(100), H9(84)
30	1 039.44	1 051.00	CH3 wagging; H25(100), H20(62)
29	1 033.46	1 043.50	ring def.; C4(100), C3(60)
28	1 011.54	1 015.00	ring def.; H24(100), C26(73)
27	998.49	997.00	CH3 wagging; H19(100), H8(91), H17(88)
26	951.63	960.50	ring def.; C1(100), H18(100)
25	948.66	952.50	ring def.; H7(100), C3(82)
24	930.78	940.50	ring def.; H8(100), H19(95), C12(88)
23	919.18	929.00	ring def.; C4(100), C3(73), H24(61)
22	897.96	906.00	ring breathing; C5(100)
21	877.54	887.50	ring breathing; C22(100), C5(99)
20	831.39	842.00	ring def.; C22(100), C4(98)

TABLE I
(*Continued*)

Mode	ω_{CAL}[a], cm^{-1}	ω_{EXP}, cm^{-1}	Mode description[b]
19	806.38	820.50	ring def.; C4(100), C1(62)
18	790.46	787.50	C=C torsion; H10(100)
17	760.70	771.50	ring def.; C22(100), C5(84)
16	656.16	665.50	ring breathing; C3(100)
15	608.54	618.50	ring breathing; C13(100), C22(79)
14	558.48	563.00	ring def.; C6(100)
13	474.54	479.50	ring def.; C26(100), C4(74)
12	454.21	462.30	ring def.; C12(100), C13(62)
11	416.26	442.00	ring def.; C22(100)
10	385.56	393.50	CH3 wagging; C12(100)
9	379.52	384.00	ring def.; C1(100), C4(91)
8	321.89	331.50	ring def.; C2(100), C14(78), C3(74)
7	297.22	302.00	CH3 wagging; C26(100), H25(42)
6	254.97		ring def.; C2(100), C13(86)
5	222.98		CH3 rot; H8(100), H19(85), H16(81)
4	198.41		CH3 rot; H25(100), H24(80), H20(76)
3	189.30		CH3 wagging; C12(100), C13(52)
2	180.81		CH3 rotation; H16(100), H17(90), H8(83)
1	125.55		CH3 wagging; C16(100), C13(53)

[a] Becke3LYP/6-31G** calculation, scaled uniformly by 0.9736; [b] relative atomic potential energies in parentheses; see Fig. 2a for atomic numbering.

Raman and ROA spectra were simulated using Lorentzian profiles of spectral bands with a uniform bandwidth of 5 cm^{-1}, matching approximately the experimental resolution.

RESULTS AND DISCUSSION

Calculated frequencies for α-pinene and *trans*-pinane, together with concise descriptions of the normal mode movements, are listed in Table I and Table II, respectively. The normal modes are highly delocalized and a description in terms of local symmetry coordinates would be problematic. Instead, we list relative kinetic energies of few atoms for each mode, which can partially complete the picture about the localization of the modes. The *ab initio* frequencies (Becke3LYP/6-31G**) were uniformly scaled by a factor of 0.9736 (0.9675) for α-pinene (*trans*-pinane), which made comparison to experimental data easier. The systematic error of frequencies is mostly attributed to

anharmonic interactions[13,14] and intermolecular interactions. The calculated frequencies are in good agreement with the experimental data. The root mean square deviation is about 10 cm^{-1} for both molecules, which is comparable with the experimental resolution. C–H stretching modes are not considered, since their ROA spectra are more difficult to obtain experimentally and the interpretation is more complicated due to the anharmonic effects, including Fermi resonances.

Calculated and experimental spectra for the two molecules are plotted in Figs 3 and 4. The top ROA spectrum (Calculation II) was calculated without the magnetic local contributions, using only the analytical derivatives of tensor α, calculated at the HF/6-31G** level. The other calculated ROA spectrum (Calculation I) also includes the local contributions to $\boldsymbol{G'}$ and $\boldsymbol{A}$ tensors. As apparent, methods (I) and (II) yield similar spectral patterns, although the complete calculation (I) gives better agreement with the experiment (as expected), namely in the low-frequency region. Due to the lower computational demand of the approximate method, we advocate the polarization model as the first test of the quality of the calculations, since the spectrum has the correct relative intensities and signs of most bands. In the experimental ROA spectra the most intense peaks are marked in accordance with Tables I and II. The *Y*-scale is arbitrary, but the same for the two upper spectra, both in Figs 3 and 4.

For both molecules we found that the simulated ROA spectra are comparable with experiment. The quality of the calculations is sufficient to distinguish between the

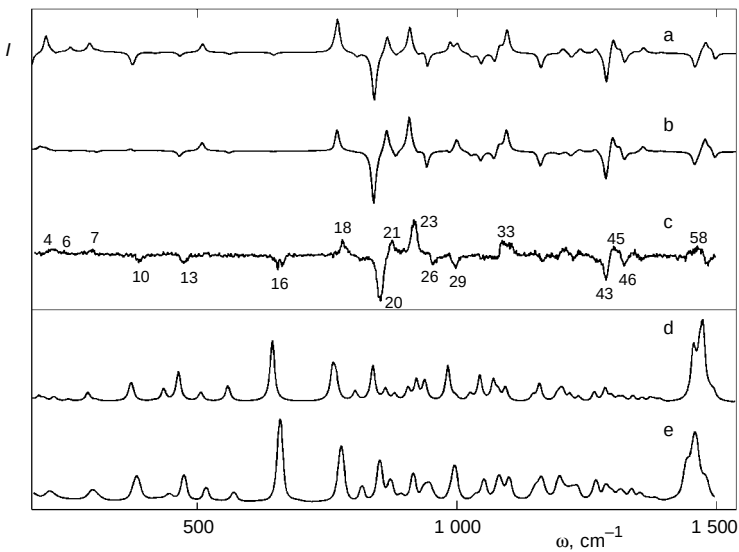

FIG. 4
Raman optical activity and Raman intensity spectra of (–)-*trans*-pinane. For description of spectral lines see Fig. 3

TABLE II
Calculated and experimental vibrational frequencies of *trans*-pinane (C–H stretching modes excluded)

Mode	ω_{CAL} [a], cm^{-1}	ω_{EXP}, cm^{-1}	Mode description [b]
60	1 488	1 482	CH bends; H12(100), H16(91)
59	1 482		H20(100), H24(98)
58	1 471		H12(100), H17(99)
57	1 469	1 459	H18(100), H19(88)
56	1 463		H26(100), H22(68)
55	1 462		H25(100), H22(67)
54	1 455	1 440	H11(100), H14(95)
53	1 450		H19(100), H12(84)
52	1 448	1 422	H21(100), H14(74)
51	1 385		H18(100), H19(100), an umbrella mode
50	1 376	1 380	H26(100), H25(98), an umbrella mode
49	1 368		H12(100), H21(100)
48	1 352	1 352	H28(100), H14(97)
47	1 334	1 336	H17(100), H13(76)
46	1 317	1 316	mixed modes: H28(100), C6(29)
45	1 308	1 308	H27(100), C3(77)
44	1 294	1 298	H28(100), H17(54)
43	1 282	1 287	H15(100), H5(100)
42	1 261	1 266	H13(100), C4(78)
41	1 231	1 232	H24(100), C9(90)
40	1 214	1 218	H17(100), H16(96)
39	1 199		C1(100), H15(37)
38	1 196	1 198	H27(100), H23(87)
37	1 189		C1(100), H13(85)
36	1 156	1 160	C1(100), C6(50)
35	1 144	1 048	C6(100), C1(90)
34	1 090	1 099	H13(100), H16(74)
33	1 076	1 080	H15(100), H28(73)
32	1 067	1 068	H13(100), C6(61)
31	1 041	1 050	H15(100), H24(85)
30	1 023	1 034	C6(100), C4(90)
29	995		H22(100), H23(71)
28	981	996	C4(100), C5(81)
27	979		H21(100), H19(83)
26	936	944	H11(100), C1(53)
25	934		C3(100), H16(71)
24	919		H20(100), H18(58)

TABLE II
(*Continued*)

Mode	ω_{CAL} [a], cm^{-1}	ω_{EXP}, cm^{-1}	Mode description [b]
23	903	916	C5(100), H23(59)
22	877	891	C5(100), C9(65)
21	860	872	C2(100), C9(99)
20	836	846	C5(100), C9(60)
19	803	817	C4(100), H24(59)
18	764	784	H16(100), H17(59)
17	759	774	C9(100), C2(94), a breathing mode
16	642	654	C8(100), C7(44)
15	556	570	C3(100), C8(53), a breathing mode
14	505	514	C6(100), C5(50)
13	463	474	C1(100), C10(95)
12	435	444	C7(100), C1(62)
11	416		C9(100), H23(45)
10	373	384	C10(100), C6(84)
9	371		C7(100), C8(52)
8	306		C3(100), H20(73), CH_3 rot
7	290	298	C10(100), C8(57)
6	253	244	H26(100), H22(99), CH_3 rot
5	224		H12(100), H18(82), CH_3 rot
4	205	220	H11(100), C7(76)
3	195		H21(100), H12(87)
2	173		C8(100), H19(65)
1	122		C2100), C10(90)

[a] Becke3LYP/6-31G** calculation, scaled uniformly by 0.9675; [b] see Fig. 2b for atomic numbering.

spectra of the two species, and the same can be said about the experiment. The success of this ROA methodology is obviously important for future applications in structural analysis. Unfortunately, although not disturbing the overall picture, some vibrational modes cannot be identified in the spectra, namely the C–H bending vibrations around 1 100 cm^{-1}. In this region, the experimental spectral peaks are poorly resolved and the density of vibrational modes is high. Moreover, signs of few weak bands in the low-frequency spectral region cannot be unambiguously determined.

The overall shape and relative intensities of the Raman spectra are reproduced well by the simulation. Although both the noise in experimental and intensity errors in calculated Raman spectra are smaller than those for ROA spectra, the latter are clearly more legible since they provide the information about the signs of the peaks. Many

Raman bands, particularly in the higher-frequency region, would be difficult to assign without the ROA spectrum, due to the band overlaps. At this stage, we feel that the simulation of the entire spectral pattern is more relevant than an analysis of individual vibrational modes, since the latter cannot be directly related to experiment.

CONCLUSIONS

Our ROA spectrometer provides high quality spectra of medium-sized optically active molecules that can be used for the determination of molecular structure. The interpretation relies on the theoretical background, since experimental and simulated spectra can be directly compared.

For α-pinene and *trans*-pinane the simulated ROA and Raman spectra are in an excellent agreement with the experiment. We found that a local origin gauge can be used for a good estimate of the ROA tensors, which reduces the computational time substantially. Calculation of the force field with the Becke3LYP/6-31G** method was a reasonable compromise with respect to the quality of results and computer cost.

The work was supported by the Grant Agency of the Czech Republic, Grant No. 203/95/0105. We thank Dr J. McCann for the help with the clarity of the text.

REFERENCES

1. Barron L. D., Hecht L.: Adv. Spectrosc., B *21*, 235 (1993).
2. Hecht L., Che D., Nafie L. A.: J. Phys. Chem. *96*, 4266 (1992).
3. Bour P., Sopkova J., Bednarova L., Malon P., Keiderling T. A.: J. Comput. Chem., in press.
4. Hecht L., Nafie L. A.: Mol. Phys. *72*, 441 (1991).
5. Polavarapu P., Bose P. K., Hecht L., Barron L. D.: J. Phys. Chem. *97*, **11211** (1993).
6. Frisch M. J.: J. Chem. Phys. *84*, 531 (1986).
7. Barron L. D.: *Molecular Light Scattering and Optical Activity*. Cambridge University Press, Cambridge 1982.
8. Hecht L., Barron L. D., Gargaro A. R., Wen Z. Q., Hug W.: J. Raman Spectrosc. *28*, 401 (1992).
9. Mistrik P.: *Thesis*. Charles University, Prague 1996.
10. Frisch M. J., Trucks G. W., Schlegel H. B., Gill P. M. V., Johnson B. G., Robb M. A., Cheeseman J. R., Kewith T., Petersson G. A., Montgomery J. A., Raghavachari K., Al-Laham M. A., Zakrzewski V. G., Ortiz J. V., Foresman J. B., Cioslowski J., Stefanov B. B., Nanayakkara A., Challacombe M., Peng C. Y., Ayala P. V., Chen V., Wong M. W., Andres J. L., Reprogle E. S., Gomperts R., Martin R. L., Fox D. J., Binkley J. S., Defrees D. J., Baker J., Stewart J. P., Head-Gordon M., Gonzales C., Pople J. A.: *GAUSSIAN 94*. Gaussian Inc., Pittsburg, PA 1994.
11. Becke A. D.: J. Chem. Phys. *98*, 5648 (1993).
12. Lee C., Yang W., Parr R. G.: Phys. Rev., B *37*, 785 (1988).
13. Pulay P.: J. Phys. Chem. *99*, 3093 (1995).
14. Tam C. N., Bour P., Keiderling T. A.: J. Am. Chem. Soc. *118*, 1025 (1996).
15. Florian J., Baumruk V., Strajbl M., Bednarova L., Stepanek J.: J. Phys. Chem. *100*, 1559 (1996).
16. Amos R. D., Rice J. E.: *CADPAC*, version 5.0. SERC Laboratory, Daresbury 1984, issue 1990.
17. Bour P.: J. Phys. Chem. *98*, 8862 (1994).
18. Bour P., Bednarova L.: J. Phys. Chem. *99*, 5961 (1995).